MicroPET Scanner Characterization

Nuno José Santos Pereira

The development of MicroPET scanners, destined to rodents and small mammals, brings clear adavantages in the clinical study of these animals, as well as in pre-clincal tests of medical prodcuts destinated to human beings. The technology transfer between these and the human PET scanners is another advantage. In the High Energy Institute of the Vrije Universiteit Brussel, one of the members of the Crystal Clear Colaboration, a MicroPET scanner prototype - ClearPET1 - with the objective of its later commercialization. This scanner is this thesis' study object. In it is made the description of the global architecture, of the detection modules, in which the phoswich matrices are the nuclear element, of the electronic modules associated with detection and of the data acquisiton and treatment system. The axial profiles of sensitivity (ASP) were experimentally determined; the comparison between experimental results and simulations done in the Gate platform, showed the agreement between these. A new method, to calculate the scattered events fraction based on ASPs is presented. Also the results of the temporal resolution calculation are presented. The data analysis tools developed throughout the experimental work part of this thesis will be useful as a basis for the caractherization of the new prototype, in a final stage: ClearPET2. The realization of improved simulations is needed to understand some unclear aspects foscued in this thesis.

Keywords: MicroPET, Sensitivity, Scatter Fraction, Coincidence Time Resolution, GATE

I. INTRODUCTION

The MicroPET scanner prototype built at VUB, ClearPET 1, is the object of study of this thesis. The physical basis of PET as well as the general characteristics of a PET scanner are presented. The architecture of the ClearPET1 is described; this description includes the detection, the electronics and the Data Acquisition (DAQ) of the scanner.

The experimental part of this work is dedicated to the sensitivity characterization of the scanner. A new method of calculating the scanner scatter fraction is presented as well as the coincidence time resolution.

II. PHYSICS

A. Positron Emission

The positron emmited in a β^+ after annihilating with its antiparticle, the electron, gives rise to the emission of two 511 keV photons in opposite directions. As a possible result of non-zero kinetic energy of the positron in the moment of annihilation, the angular deviation between the two photons is represented by a gaussian curve with an average of 180° and a FWHM of 0.5^o.

These two photons are the physical observables in which PET techniques rely on. The photons interact with matter mainly by Compton Scattering, as this is the dominant interaction process at photon energies of $\sim$ 511 keV.

B. isotopes

Being a functional imaging technique based on positron emission, the activity of a given part of the body is traced by the amount β^+ decays and consequent 511 keV gammas emission. Is thus necessary to introduce in the body elements decaying by β^+ like ^{18}F, ^{11}C or ^{15}O refs 2 and 4. This is done by chemically linking these elements with organic molecules like serotonin or glucose. By linking an ^{18}F atom to a glucose molecule, one obtains the radioactive compound $^{18}F - FDG$, the most widely used in oncology.

C. Photon Detection

To detect the photons emmited in the positron-electron pair annihilation, scintillator crystals are used.

In PET inorganic scintillators are used; this type of scintillators have a high Z_{eff} to achieve a good detection efficiency. A large efficiency is a desired chracteristic.

The detection of scintillation light and its conversion to a current pulse is made by a Photmultiplier Tube (PMT). Scintillation photons hit the PMT photocathode and electrons are ejected from it by photoelectric effect; this process has an intrinsic efficiency: Quantum Efficiency. The photoelectrons are then sucessively multiplied in the PMTs dynodes until they reach the anode, when an electrical pulse is produced. The number of secondary photoelectrons is related with the voltage applied by eq. (1)

$$G = V^n \tag{1}$$

The energy resolution of an energy spectrum is measured with respect to a photopeak. Because photopeaks are Gaussian-shape like, rather than vertical lines, the energy resolution is given by the width at half height of the this gaussian. Thus the energy resolution is given by eq. (2)

$$R_{FWHM} = \frac{\Delta E_{FWHM}}{E} \tag{2}$$

III. EVENTS

The PET imaging techniques rely on the accurate determination of the two photons originated in the same e^+e^- annihilation, a coincidence.

Coincidences are distinguished between real coincidences, when the two detected photons are originated in the same annihilation; scatter coincidences, when, at leat, one of the annihilation photons suffers Compton interaction(s) before being detected; random coincidence, when the two detected singles are originated in different annihilations. Fig. 1 illustrates this.

Due to the system's temporal resolution, a valid coincidence requires that photons are detected in opposite detectors, within a specified time window. This time window is tipically of the order of nanoseconds. Random coincidences are estimated with a delayed time window process: a time window(τ) is open, not immediatly after the detection of the first photon, but after a certain delay time ($d \gg \tau$). This takes to the lose of temporal correlation between the

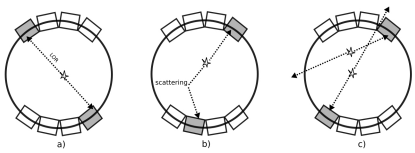

FIG. 1: a)true coincidence; b)scatter coincidence; c)random coincidence

two photons and instead of a possible true coincidence, a random coincidence is detected.

IV. PET SCANNER CHARACTERISTICS

A. Sensitivity

The sensitivity of a PET scanner expresses the ratio between detected coincidences and the total number of β^+ decays that undergo pair annihilation given by eq. (3). It is strongly dependent on the detection efficiency as well as on the scanner geometry.

$$sensitivity = \frac{N_{detected}}{N_{\beta+}} \tag{3}$$

B. Noise Equivalent Count

Noise Equivalent Count expresses the relation between useful and noisy signal of a PET scanner, its expression is given by eq. (4)

$$NEC = \frac{T^2}{T + S + 2R} \tag{4}$$

Where T, S and R stand for true, scatter and random coincidences, respectively. NEC curves are expressed as a function of radioactivity, and allow to estimate the optimal relation between usfeul and noisy signal.

C. Spatial Resolution

Spatial Resolution translates the minimum distance between two points in the same image that a system can distinguish between. In a PET scanner this is particulary important in the sense that one is interested in detecting the possible smallest disease. Some factors contribute to the degradation of spatial resolution:

- the fact that the positron travels a finite distance between the production and annihilation spots.
- the non-collinearity of the emmited photons.
- the parallax error, this is due to the impossibility in determining the exact spot where a photon hits the scintillation crystal; this error is thus proportional to the crystal dimensions and in practice one reduces it by using more than one crystal layer with smaller dimensions.

D. Time Resolution

A PET scanner time resolution is a measure of how accurate the arrival time of one photon is determined. The determination of the coincidence time resolution is also done by computing the differences of arrival times of coincidence photons. This distribution is a shape-like gaussian, for which the coincidence time resolution can be measured as the FWHM of it. Time resolution and coincidence time resolution are related by eq. (5)

$$Coincidence\ time\ resolution = \sqrt{2}\ Time\ resolution \tag{5}$$

V. CLEARPET1 SCANNER

ClearPET1 prototype was built at VUB and used for trials in Ghent University. It has an inner diameter of 143mm. Eight detection modules (cassettes) are disposed radially, being four of them diametrically opposing the other four.

A. Detection Modules

1. *Scintillation Crystals*

Two types of scintillation crystals are used: LSO and LuYAP. The dimensions of each individual crystal are 2x2x8 mm^2. There is a total of 128 crystals mounted in two layers of an 8x8 *Tyvek* matrix. LSO crystals present a light yield (LY) about 4 times larger than LuYAP crystals. Setting a low discrimination value to the light pulses, would favorish undesired low energy Compton events and multiple triggering events provoked by cross-talk. It is thus necessary to uniformize both crystal layers LYs. Three solutions are adopted to accomplish this:

- the LuYAP crystals light collection efficiency is raised by a factor 2, by directly gluing it to the photodetector window.
- LSO LY is decreased to a value 10% to 30% lower than LuYAP one by placing a sheet of *Mylar* in between both crystal layers
- LSO LY is increased by placing a light-reflecting paper in the outer face of LSO crystals.

2. *Photo Multiplier Tubes*

The Photo Multiplier Tubes (PMTs) used to detect scintillation light are Multi-Anode HAMAMATSU R7600-M64. They have a sensitive area of 18.1x18.1 mm^2 readout by a matrix of 64 cathodes, each having a surface of 2x2 mm^2 that matches the dimensions of the crystals surface, working thus as individual detector pixels. There are 64 individual anode outputs, as well as a common dynode output corresponding to the analog sum of the 64 individual pixels.

Phoswich matrix is the name given to the ensemble of both crystal layers and PMT.

3. *cassettes*

The dimensions of the cassette are 25x15x4 cm^3. It is made out of aluminium and is the physical support to the detection and readout electronic modules. A box in the front of the cassette houses the light sensitive part of the scintillation crystals and PMTs; it is black in order to prevent these from direct light exposition.

B. Electronics

Each detection cassette contains the following components: two phoswhich matrices, two decoder blocks, one FPGA, one slow control board and an optical link.

1. Decoder Block

Each decoder block consists of 64 comparators connected to PMT anodes, an address decoder of the anodes and a dynode signal preamplifier. The comparators are triggered if, at least, one anode signal exceeds a threshold value; this threshold value is common to the 64 channels and can differently be set for each PMT. When a trigger occurs the amplified dynode signal and the adresse(s) of hit pixel(s) are sent to the FPGA board

2. FPGA Board

The FPGA board holds an FPGA and four free running 12-bit ADCs at 40 MHz. This 40 MHz is set by an external clock synchronous for all cassettes. When a trigger event occurs, 16 samples of the incoming dynode signal are saved.

The FPGA takes 700 ns to process each trigger event; this time is the biggest contribution to the **dead time** of the system. The 40 bytes of data are sent to a Data Acquisition computer via an optical link interface.

3. Slow Control Board

The slow control board is situated in the back part of each cassette; it is equipped with a microcontroller that adjusts High Voltage (HV) and threshold, individually, for each PMT. HVs are generated by DC-DC converters. HV and threshold settings are received from a Master PC, via a RS232 serial interface. Additionally, the microcontroller monitors the HVs and supply voltages as well as the temperature given by a sensor placed near the phoswhich matrix.

4. Optical Link

In the top of the slow control board is placed a piggyback board with an optical transceiver unit but it is set to works only as a data transmitter; it sends 16 bits data words to a Slave PC at a rate of 10 MHz.

C. Data Acquisition

The DAQ of the scanner consists of one Master PC, two Slace PCs and a Data Storage PC. The communication between them is realised by socket connections at 1 GBit/s.

1. Slave PC

The data flow from from the eight cassettes is received by two Slave PCs. Each Slave PC holds two interface boards with two I/O cards each. Each I/O card holds the same piggyback boards as the optical link, this time using the receivers only. The 32-bit port of each I/O cards is configured as two 16-bit independent ports; one card is then able to receive data from two cassettes. The data transfer made up to a rate of $450 \times 10^3 events/s$.

For each event received from a cassette the Slave PC processes the raw data and computes the following:

Energy
energy of the pulse is given by the sum of the 16 digitized pulse samples, after pedestal subtraction

Time Mark
a straight line is fitted into the two points for which the slope is maximum; the intersection of this line with the baseline of the pulse is considered the new event time mark. This method improves the scanner's temporal resolution from 25 ns to 4.2 ns [11]

DOI
the depth of interaction information, i.e., the information whether the crystal layer where the trigger event was produced is LSO or LuYAP layer is determined using a method called Pulse Shape Discrimination, based on the presence of a slow decay component of LuYAP scinitllation pulse. This PSD method has a reliability of 97%. [8].

2. Master PC

The Master PC is responsible for controlling all the scan processes. It runs a LabView application that manages a Graphical User Interface (GUI) allowing to control the parameters of the acquisition such as time of acquisition, bed position and gantry rotation.

VI. RESULTS

A. Sensitivity

In the sensitivity characterisation of the scanner one first presents the comparison between simulated and measured data for the Axial Sensitivity Profile of the scanner 2

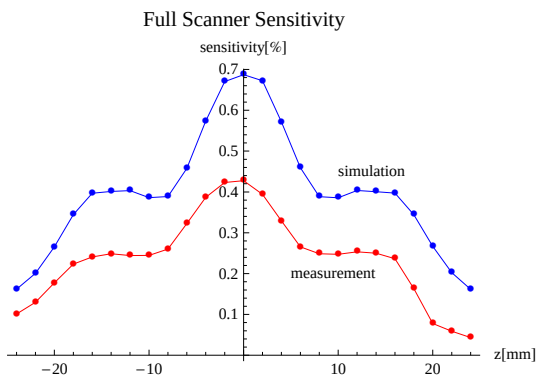

FIG. 2: PMTs measured singles rate compared with simulation. Left: level 0 PMTs. Right: level 1 PMTs

Simulated and measured sensitivity values are not in agreement; the highest sensitivity points are 0.69% and 0.43% for simulation and measurement respectively; this means a lost of ∼38% in measured sensitivity. Simulated total sensitivity is 42% higher than measured one.

Measured curve also presents an asymmetry relative to the y axis and an asymmetry between the first four and the last four measured z positions.

1. PMT singles rate

For each PMT the measured and simulated singles rate were calculated by eq (6)

$$rate\left[s^{-1}\right] = \frac{singles}{t_{acquisition}} \tag{6}$$

Fig. 3 shows the singles rates for each PMT along the z axis of the scanner.

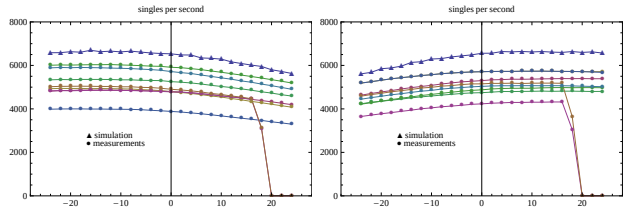

FIG. 3: PMTs measured singles rate compared with simulation. Left: level 0 PMTs. Right: level 1 PMTs; for clearness of visualisation, only one simulated PMT is shown, as simulated single count rate per PMT is practically equal

One can see that, for the four PMTs of cassettes 11 and 12, there are bad data points, between 18 mm and 24 mm. Indeed, the *log files* of the measurement show that between those specific positions, there are no counts for these four specific PMTs, due to an error in data acquisition.

The real PMT that agrees best with simulation is PMT 0 of cassette, with a 91% ratio. The PMT with a worst agreement is PMT 1 of cassette 11, with a ratio of 56%. The average of all the ratios is 75% ± 11%.

The bad data points previously noted explain the asymmetry in the measured curve in fig. 2.

In order to explain this average difference of 25% in singles rate between simulation and measurements, some issues were identified as possible factor of disagreement: factors where simulation doesn't include some phenomena taking place in the real system, and also factors where simulation does not take into account the variations on performance of components of the same type, specifically the PMTs.

a. Real PMT Characteristics

In simulation PMTs thresholds are set to a sharp defined value; in this specific work this value is set to 250 keV. This precision is not possible in the real system due to the energy calibration method used. The simulated energy resolution is 22.9%.

The average measured threshold level is 249 keV±16%. The average energy resolution is 34.8%±5.4%.

b. LSO Background

LSO crystals contain approximately 2.6% of ^{176}Lu [10], a natural occurring radioisotope that is a γ emitter. Its influence on single count rates has been measured and is not negligible [9]; LSO background is not simulated. This background radioactivity accounts with ∼ 10% to the measured singles count rate.

c. Position and Energy Errors

During measurements, errors in determining the index of the pixel hit, *fars* and *errors of position*, and *errors of energy* are expected to happen. In the simulation these errors are not included. The *log files* of the acquisition show an average of 10.5% of errors over the total single count.

We assume that the bad results between the simulated and measured count rates of PMTs shown in fig. 3 have its origin in the following reasons:

- The contribution of the LSO background that underestimates the simulation count rates by ∼10% is not negligible.
- The average threshold level of real PMTs, 249 keV, which is good result compared with the 250 keV threshold level set in simulation; its dispersion of ∼16% is expected, giving the method used to experimentally set it, explained before.
- The contribution of the bad events to the loss of counts in the real system, altough its origin is not clear, can be quantified; for each PMT there is a fairly constant percentage of this error, over all the measured z positions. In average ∼11% of the singles are bad events; these are not accounted in simulation.
- In spite of not having influence in the singles count rate, an over-estimated average of 34.8% is fairly worse than a energy resolution of 22.9% for simulation.

For the characterisation in sensitivity of the scanner, the previous discussion will be taken into account; because setting the individual characteristics of each PMT is not feasible in simulation, the method used is to adapt the simulated to the measured data: The simulated count rate will be scaled to its respective PMT in the real system; the scaling factors shown are defined individually for each PMT; each one of these corresponds to the measured/simulation ratio, averaged over the all z positions. In them it is included the contribution of all the disagreeing parameters discussed before.

In the coincidence sorting algorithms for simulated data, for the specific PMT pairs for which coincidences are detected, a fraction of the singles events are rejected, via a random selection, according to the singles rate scaling factor for each PMT.

2. PMT Pair Coincidence Sensitivity

The following analysis will be the characterisation in sensitivity for coincidences of a PMT pair, from opposite cassettes. Only coincidences between same index PMTs (PMT0-PMT0 or PMT1-PMT1) are considered,.

Fig. 4 shows the sensitivity profiles for all same level PMT combinations for all pair of opposite cassettes.

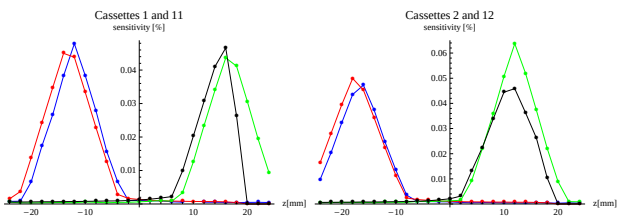

FIG. 4: Simulated and measured sensitivity for PMT pairs. Blue: simulation PMTs index 0. Red: measurement PMTs index 0. Green: simulation PMTs index 1. Black: measurement PMTs index 1. Only cassette pairs 1-11 and 2-12 are shown.

3. Cassette Pair Coincidences Sensitivity

The sensitivity to coincidences for all pair of opposite cassettes will now be analysed; all coincidences for a specific cassette pair are accepted.

In fig. 5 the sensitivity profiles for the four pair of opposite cassettes are shown; z position for measured data is corrected for each cassette pair with the respective peak deviations.

The lateral peaks of the profile show the contribution of same index PMT sensitivity shown in fig. 4; The central peak expresses the sensitivity for the coincidences occurring between PMTs of different index.

Left and right peaks of each profile show an expected behaviour when compared to the respective peaks of fig. 4: there is a maximum difference of 4% between respective left and right peak ratios.

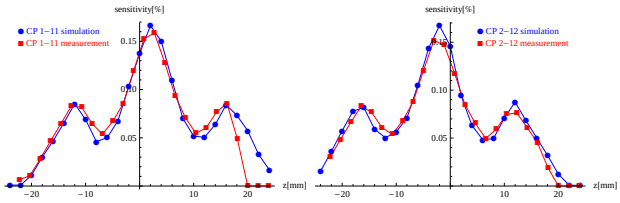

FIG. 5: Blue: simulated sensitivity profile. Red: measured sensitivity profile; the z position for each one of the cassette pair plots is corrected for the respective peak deviation. Only cassette pairs 1-11 and 2-12 are shown

The averaged central peak and total sensitivity ratios are, respectively, 0.96±0.07 and 1.04±0.11.

These numbers shows that a consistent agreement in cassette pair sensitivity with the results for PMT pair sensitivity.

4. *Full Scanner Sensitivity*

The sensitivity of the full scanner will now be recalculated. Results for the simulated and the measured sensitivity profiles are shown in fig. 6.

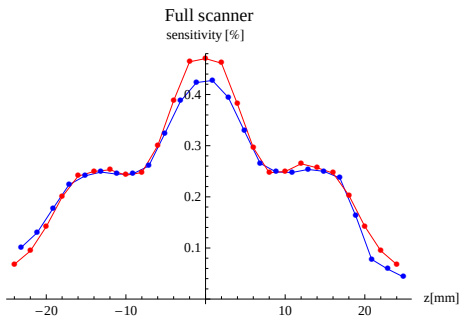

FIG. 6: Blue: simulated sensitivity profile. Red: measured sensitivity profile. The axial position of measured data is corrected as the average of all the peaks deviations

A good agreement between measured and simulated total sensitivity is seen, with a measured to simulation ratio of 96%. The central (z=0 mm) position, corresponding to the point of the scanner's maximum sensitivity shows an improvement of the agreement between measurement and simulation, with ratio of 91%.

5. *Scatter Fraction*

In this work a method of estimating scatter fraction using sensitivity profiles will be presented. The following points have to be considered when using this method:

- to calculate a full scanner sensitivity coincidences from all PMT combination are accepted; a fraction of this coincidences are due to scattered events in the scanner's material, such as the metallic parts of the rotation gantry, the cassettes and the animal bed.
- the source is positioned at the central line of the scanner ($x = 0$ $y = 0$), so that the scattered coincidences are the ones occurring in non opposite cassette pairs.
- when calculating cassette pair sensitivity, only coincidences from the specific cassette pairs are accepted.

Taking into account the previous considerations, one concludes that the scattered coincidences are the difference between coincidences detected for the full scanner's sensitivity (fig. 6) and the sum of coincidences detected for the cassette pair sensitivity profiles (fig. 5).

In fig. 7 is shown the full scanner sensitivity profile and the sum of the four individual cassette pair sensitivity profiles.

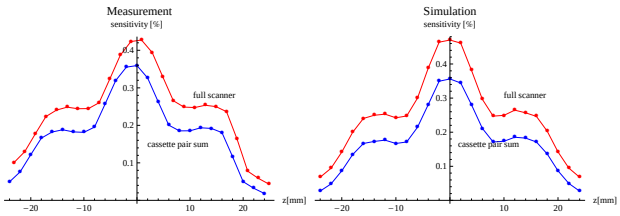

FIG. 7: comparison between full scanner and cassette pair sum sensitivity profiles, for measurement and simulation

The number of scattered coincidences is then the difference between red and blue curves. In fig. 8 (left) this difference is expressed in sensitivity; in fig. 8 (right) is shown the scatter fraction.

$$SF\,[\%] = \frac{scattered_{coin}}{total_{coin}} \tag{7}$$

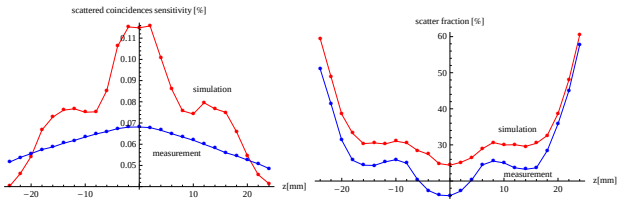

FIG. 8: left: scattered coincidences contribution to sensitivity; right: scatter fraction

Fig. 8 (left) shows a fairly uniform distribution of scattered coincidences along the z axis, for measured data, while simulated one shows a similar shape profile to the scanner sensitivity profile. This seems to indicate a dependency on the scanner geometry for the simulated data. This can be explained by the fact that, in simulation, structural elements such as the bed or the metallic rotation gantry are not modeled. The scattered events occurring in these elements, in the real system, can explain the totally different distribution of scattered events for simulated and measured data along the FOV of the scanner.

Fig. 8 (right) shows a good agreement in shape between scatter fraction curves, despite the fact that the profile of the number of scattered coincidences is very different for measurement and simulation.

Scatter fraction is minimum in the centre of the FOV with 24% and 16%, respectively for simulation and measurement. In the extreme points of the FOV it can go up to 60% both for simulation and measurement; this SF curve would eventually reach 100% for even more extreme positions of the FOV, as the solid angle for real coincidences tends to zero.

a. *Scatter Fraction Correction*

Assuming that in the simulation the scattered events are well modeled, and that the difference with measurements is due to the fact that the structural elements referred before are not modelled, we can apply a correction to the full scanner's sensitivity profiles of both measurement and simulation: each sensitivity profile will be corrected for the corresponding fraction of scattered events. With this correction one obtains the full scanner's sensitivity profile for true coincidences shown in fig. 9:

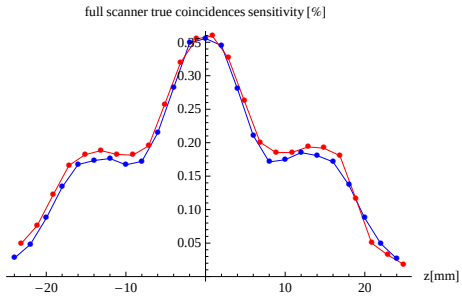

FIG. 9: Blue: simulated sensitivity profile. Red: measured sensitivity profile

After scatter fraction correction, the ratios between measured and simulated sensitivity are 1.01 for the highest sensitivity point (z=0 mm) and 1.07 for the total sensitivity along the scanner's z axis.

These numbers show that, altough we cannot exhaustively modelate the PMT behaviour in simulation, the adaptation of simulation PMT singles rate to measured singles rate revealed itself as a good method to characterise the scanner in sensitivity.

The consistently higher simulated singles rate could qualitatively be explained by analysing the real system PMT characteristics; the influence of non simulated phenomena - LSO background and *bad events* - in the difference of count rares could be quantified. The PMT pair sensitivity analysis was useful to measure the mispositioning of PMTs. The correction of the full scanner's sensitivity profile to the scattered coincidences brought simulation and measurement to a better agreement, altough the scatter events distribution (fig. 8) is not fully understood.

B. Coincidence Time Resolution

The results for determining the coincidence time resolution of the scanner will be presented now.

Coincidence time, (Δt_{coin}), is defined as the difference between the arrival times of two coincidence photons. The arrival time mark is calculated as explained in sec.3.4. The photon's arrival time distribution has a Gaussian shape, implying that Δt_{coin} distribution also has a Gaussian shape.

Fig. 10 shows Δt_{coin} distribution, for four PMT pairs combination; the fact that these distributions are not centred in 0, is due to the different transit times in PMT and/or electronics [3]. The average position of the distribution is presented as well as the time resolution for each distribution.

All of the above distributions show an asymmetry in the tails of the Gaussian curve; this asymmetry is related with the difference of incoming pulse shapes [7].

By summing the distributions of all the PMT pair combination of a pair of opposite cassettes, one obtains the Δt_{coin} for a cassette pair; also the different delays presented for each distribution are taken into account, as each distribution average is shifted towards zero. Fig. 11 shows the summing of the four distributions of one cassette pair; the LSO and LuYAP resolutions are also plotted.

One can see that LuYAP energy resolution is systematically worst than LSO one. The explanaition for this fact is related with the difference in determining the arrival times of pulses with similar shapes, but with different amplitudes [7]. Pulses with a lower amplitude, this is the case if LuYAP and LSO LYs are compared, show an higher dispersion in determining the arrival time, leading to worst time resolutions.

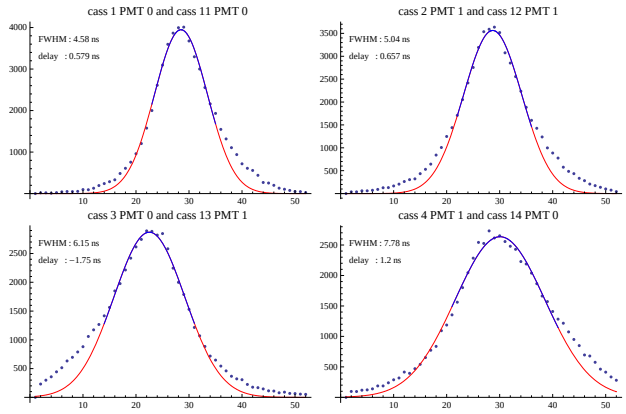

FIG. 10: For each PMT pair combination of each cassette pair Δt_{coin} is plotted; only the points with a Gaussian like shape (blue points) are used to fit a Gaussian distribution; the average of this distribution is presented as a delay and the FWHM as the time resolution

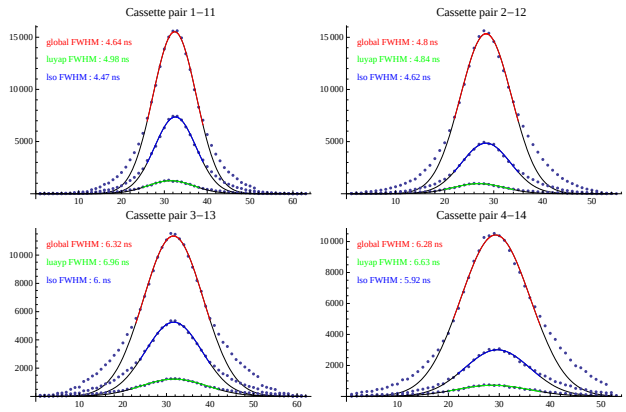

FIG. 11: Global and crystal layer energy resolutions for each opposite cassette pair; the blue curve refers to LSO-LSO interactions and the Green curve refers to LuYAP-LuYAP interactions

By adding the Δt_{coin} distributions for the four cassette pair combinations one obtains the time resolution for the whole scanner shown in fig. 11.

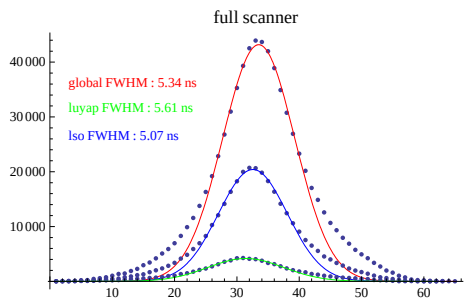

FIG. 12: full scanner time resolution

The global coincidence time resolution of the scanner is 5.34 ns, while time resolutions for LSO and LuYAP layers are 5.07 ns and 5.61 ns, respectively. Using eq. (5) one obtains a time resolution of 3.77 ns.

VII. CONCLUSIONS

The results obtained for the sensitivity of the scanner can be considered satisfactory. The good agreement between measured data and GATE simulations could be observed for PMT pair, cassette pair and full scanner sensitivity. The measured and simulated full scanner sensitivity for the highest sensitivity point were 0.36% and 0.35%, respectively.

Not only the results were satisfactory but, more important, the methods used for characterising the scanner's sensitivity lead us to a better understanding of the scanner. One was able to evaluate the different performances of the nuclear component of the detection system: the phoswhich matrix.

The energy resolutions showed a big deviation relatively to simulation: the best real system energy resolution was significantly worse than the simulated one, with respective values of 28.1% and 22.9%. The measured threshold energies of the PMTs were in a good agreement with simulation, with an average value of 249 keV, while simulated threshold was of 250 keV. The influence of LSO background was well determined: it contributed not only to an increase in the measured singles count rate, but it also had influence in the energy resolution determination. In the inverse way, the amount of bad events contributed to a decrease in the measured count rates; the origin of these errors in the real system is not clear, but its contribution to the measured singles decrease is well known for each PMT. A much lower contribution to the measurement/simulation disagreement was detected: small deviations in the positioning of PMTs were measured, as well as the existence of a systematic error of 0.86 mm in determining the real position in measurements.

A new method of determining the scatter fraction using sensitivity profiles was presented. The results show a similar behaviour between measured and simulated scatter fraction. The variation of the SF between the centre and the extreme positions of the FOV was of 24% to 60% and 16% to 50% for simulation and measurement, respectively.

All the previously described factors will be useful in future work on the second version of the ClearPET; ClearPET2 differs from ClearPET1 in the crystals height and in the number of PMT per cassette: it will have 8 mm long crystals and 4 PMTs per cassette. In spite of that, the methods used to calculate PMT energy resolutions and thresholds remain valid in the new scanner.

The future simulations relative to the new scanner can also be improved, taking into account the issues shown previously and that were not modeled in simulations used in this work.

The measured global time resolution of the scanner is 5.34 ns. The time resolutions of LSO and LuYAP crystal layers were also calculated and are 5.07 ns and 5.61 ns, respectively; the lower time resolution of LSO compared to LuYAP was expected, given the difference in the light yield of both crystals.

The time resolution between PMT pairs were also calculated; an unexpected asymmetry in the coincidence time distribution was detected, but its origin was related with the difference in pulse shapes.

[2] S. Tavernier. **Measurement Techniques in Nuclear and Particle Physics**. VUB 2007

[3] S. Tavernier et all. **First Results with the ClearPET Small Animal PET Scanners**. Radiation Detectors for Medical Applications. 2006 Springer

[8] M.Streun et all. **Pulse Shape Discrimination of LSO and LuYAP. Scintillators for Depth of Interaction Detection in PET**. IEEE Transactions on Nuclear Science; vol.50, no.3, June 2003

[5] U. Heinrichs **Auslegung Des Detektorsystems Fur Einen Hochauflosenden Positronen-Emissions-Tomographen Mit Hoher Sensitivitat**. Forschungszentrum Julich, Zentralbibliothek, 2003

[6] S. Jan et all. **GATE: GEANT4 Application for Tomographic Emission: a simulation toolkit for PET and SPECT**. http://opengatecollaboration.org. 2006

[7] Knoll G. **Radiation Detection and Measurement**. John Wiley sons, 1999

[8] M.Streun et all. **Pulse Shape Discrimination of LSO and LuYAP. Scintillators for Depth of Interaction Detection in PET**. IEEE Transactions on Nuclear Science; vol.50, no.3, June 2003

[9] S. Yamamoto. *Investigation of single, random and true counts from natural radioactivity in LSO-based clinical PET.* Annals of Nuclear Medicine Vol.19, No.2, 109-114, 2005

[10] J.S.Huber et all. **Effect of ^{176}Lu background on singles transmission for LSO-based PET Cameras**. Physical Medical Biology. 47 (2002) 1-7

[11] M. Streun et all. **The Data Acquisition System of ClearPET Neuro-a Small Animal PET Scanner**. IEEE Transactions on Nuclear Science, Vol.53, no.3, June 2006

[12] S. Derenzo. **Mathematical removal of positron range blurring in high resolution tomography**. IEEE Transactions on Nuclear Science, Vol.33 pp:565-569, 1986.